

Automatic Diagnosis of Cancer Using Machine Learning

Lead Guest Editor: Abdullah-Al Nahid

Guest Editors: Mehedi Masud, M. A. Parvez Mahmud, and Anupam Kumar
Bairagi





Automatic Diagnosis of Cancer Using Machine Learning

Automatic Diagnosis of Cancer Using Machine Learning

Lead Guest Editor: Abdullah-Al Nahid

Guest Editors: Mehedi Masud, M. A. Parvez
Mahmud, and Anupam Kumar Bairagi



Copyright © 2021 Hindawi Limited. All rights reserved.

This is a special issue published in "Journal of Healthcare Engineering." All articles are open access articles distributed under the Creative Commons Attribution License, which permits unrestricted use, distribution, and reproduction in any medium, provided the original work is properly cited.

Associate Editors

Xiao-Jun Chen , China
Feng-Huei Lin , Taiwan
Maria Lindén, Sweden

Academic Editors

Cherif Adnen, Tunisia
Saverio Affatato , Italy
Óscar Belmonte Fernández, Spain
Sweta Bhattacharya , India
Prabadevi Boopathy , India
Weiwei Cai, USA
Gin-Shin Chen , Taiwan
Hongwei Chen, USA
Daniel H.K. Chow, Hong Kong
Gianluca Ciardelli , Italy
Olawande Daramola, South Africa
Elena De Momi, Italy
Costantino Del Gaudio , Italy
Ayush Dogra , India
Luobing Dong, China
Daniel Espino , United Kingdom
Sadiq Fareed , China
Mostafa Fatemi, USA
Jesus Favela , Mexico
Jesus Fontecha , Spain
Agostino Forestiero , Italy
Jean-Luc Gennisson, France
Badicu Georgian , Romania
Mehdi Gheisari , China
Luca Giancardo , USA
Antonio Gloria , Italy
Kheng Lim Goh , Singapore
Carlos Gómez , Spain
Philippe Gorce, France
Vincenzo Guarino , Italy
Muhammet Gul, Turkey
Valentina Hartwig , Italy
David Hewson , United Kingdom
Yan Chai Hum, Malaysia
Ernesto Iadanza , Italy
Cosimo Ieracitano, Italy

Giovanni Improta , Italy
Norio Iriguchi , Japan
Mihajlo Jakovljevic , Japan
Rutvij Jhaveri, India
Yizhang Jiang , China
Zhongwei Jiang , Japan
Rajesh Kaluri , India
Venkatachalam Kandasamy , Czech Republic
Pushpendu Kar , India
Rashed Karim , United Kingdom
Pasi A. Karjalainen , Finland
John S. Katsanis, Greece
Smith Khare , United Kingdom
Terry K.K. Koo , USA
Srinivas Koppu, India
Jui-Yang Lai , Taiwan
Kuruva Lakshmanna , India
Xiang Li, USA
Lun-De Liao, Singapore
Qiu-Hua Lin , China
Aiping Liu , China
Zufu Lu , Australia
Basem M. ElHalawany , Egypt
Praveen Kumar Reddy Maddikunta , India
Ilias Maglogiannis, Greece
Saverio Maietta , Italy
M.Sabarimalai Manikandan, India
Mehran Moazen , United Kingdom
Senthilkumar Mohan, India
Sanjay Mohapatra, India
Rafael Morales , Spain
Mehrbakhsh Nilashi , Malaysia
Sharnil Pandya, India
Jialin Peng , China
Vincenzo Positano , Italy
Saeed Mian Qaisar , Saudi Arabia
Alessandro Ramalli , Italy
Alessandro Reali , Italy
Vito Ricotta, Italy
Jose Joaquin Rieta , Spain
Emanuele Rizzuto , Italy

Dinesh Rokaya, Thailand
Sébastien Roth, France
Simo Saarakkala , Finland
Mangal Sain , Republic of Korea
Nadeem Sarwar, Pakistan
Emiliano Schena , Italy
Prof. Asadullah Shaikh, Saudi Arabia
Jiann-Shing Shieh , Taiwan
Tiago H. Silva , Portugal
Sharan Srinivas , USA
Kathiravan Srinivasan , India
Neelakandan Subramani, India
Le Sun, China
Fabrizio Taffoni , Italy
Jinshan Tang, USA
Ioannis G. Tollis, Greece
Ikram Ud Din, Pakistan
Sathishkumar V E , Republic of Korea
Cesare F. Valenti , Italy
Qiang Wang, China
Uche Wejinya, USA
Yuxiang Wu , China
Ying Yang , United Kingdom
Elisabetta Zanetti , Italy
Haihong Zhang, Singapore
Ping Zhou , USA





Contents

Chest CT Findings and Differential Diagnosis of *Mycoplasma pneumoniae* Pneumonia and *Mycoplasma pneumoniae* Combined with Streptococcal Pneumonia in Children

Jing Wang , Chen Xia , Ashutosh Sharma , Gurjot Singh Gaba , and Mohammad Shabaz 

Research Article (10 pages), Article ID 8085530, Volume 2021 (2021)

Boosting Breast Cancer Detection Using Convolutional Neural Network

Saad Awadh Alanazi , M. M. Kamruzzaman , Md Nazirul Islam Sarker , Madallah Alruwaili ,

Yousef Alhwaiti , Nasser Alshammari , and Muhammad Hameed Siddiqi

Research Article (11 pages), Article ID 5528622, Volume 2021 (2021)

Research Article

Chest CT Findings and Differential Diagnosis of *Mycoplasma pneumoniae* Pneumonia and *Mycoplasma pneumoniae* Combined with Streptococcal Pneumonia in Children

Jing Wang ¹, Chen Xia ¹, Ashutosh Sharma ², Gurjot Singh Gaba ³,
and Mohammad Shabaz ⁴

¹Department of Infectious Diseases, Children's Hospital of Nanjing Medical University, Nanjing, Jiangsu 210008, China

²Institute of Computer Technology and Information Security, Southern Federal University, Rostov-on-Don, Russia

³School of Electronics and Electrical Engineering, Lovely Professional University, Phagwara 144411, India

⁴Arba Minch University, Arba Minch, Ethiopia

Correspondence should be addressed to Chen Xia; xiachen1020@outlook.com and Mohammad Shabaz; mohammad.shabaz@amu.edu.et

Received 7 April 2021; Revised 22 May 2021; Accepted 2 June 2021; Published 15 June 2021

Academic Editor: Anupam Kumar Bairagi

Copyright © 2021 Jing Wang et al. This is an open access article distributed under the Creative Commons Attribution License, which permits unrestricted use, distribution, and reproduction in any medium, provided the original work is properly cited.

Background. In this day and age, 17% of children less than 5 years of age died of pneumonia; it is the common cause of children death. It is one of the main children respiratory infectious diseases, i.e., mycoplasma pneumonia (MP). The imaging examination can be adopted to quickly observe the morphology and scope of the pulmonary lesions and know the effect of disease treatment and subsequent changes in the disease in order to provide a basis for treatment. Therefore, the most commonly applied technology for detecting pneumonia in children is imaging technology, including chest X-ray and CT. **Objectives.** The main objective of the work is to investigate the chest computed tomography (CT) findings of children patients with *Mycoplasma pneumoniae* pneumonia (MPP) and MP combined with streptococcal pneumonia (SP). The mixed infection of MP and SP is very common clinically, and the diagnosis of this type of mixed pneumonia is a critical research topic faced by pediatric respiratory physicians. The comparison is done on the incidence of bronchial and pulmonary interstitial lesions, the degree of lymph node enlargement, the volume and depth of pleural effusion, and the location and morphology of the pulmonary lesions in the chest CT images of children patients from the two groups. **Methods.** There were comparisons on the incidence of bronchial and pulmonary interstitial lesions, the degree of lymph node enlargement, the volume and depth of pleural effusion, and the location and morphology of the pulmonary lesions in the chest CT images of children patients from the two groups. All the experiments are done in the MATLAB. **Results.** The results showed that the proportions of reticular shadow, ground glass shadow, bronchial inflation phase, tube wall thickening, and vascular bundle thickening on the CT images of children patients from the MPP group were dramatically higher than those of the MP + SP group ($P < 0.05$). The maximum transverse diameter of enlarged lymph node in children patients from the MPP group was obviously larger than the diameter of the MP + SP group ($P < 0.05$). The number of children patients with pleural effusion was 22 in the MP + SP group, which was greatly higher than the MPP group ($P < 0.05$). **Conclusion.** In conclusion, the chest CT images of children patients from the MPP group were mainly pulmonary interstitial changes. Furthermore, the alveolar inflammation could be observed on the CT images shown when children patients were combined with SP infection. The more obvious manifestations were that the flaky shadows appeared in the lungs, the pleural effusion became thicker, and the transverse diameters of enlarged lymph nodes were bigger.

1. Introduction

Childhood pneumonia is the main cause of death for children under the age of 5 years, and SP is the most common type of pneumonia from the 20th day of birth to the entire childhood. The MP infection rate in children that are older than 5 years old is more than 50% [1]. The mixed infection of MP and SP is very common clinically, and the diagnosis of this type of mixed pneumonia is a critical research topic faced by pediatric respiratory physicians. Accurate imaging diagnosis can help clinicians to treat the disease in time and use drugs rationally, so as to avoid delay in the conditions of patients.

Nowadays, 17% of children less than 5 years of age died of pneumonia; it is the common cause of children death [2, 3]. It is one of the main children respiratory infectious diseases, that is, mycoplasma pneumonia. In the initial age, there may or may not be clinical symptoms which cause the lesions outside the respiratory system. Several days are required for the completion of the serologic diagnosis for making decision of initial medication which is critical for the community-acquired pneumonia treatment [3]. The images for childhood pneumonia and the fight against pneumonia are shown in Figure 1.

Pneumonia is the most frequent disease and its main causes are pathogen infection and body allergic reactions. In the past 3 years, MPP has become a common pneumonia in children and adolescents, accounting for 10%–40% of community-acquired pneumonia, and its infection rate is 10%–20% [4, 5]. Compared with simple MP, combined SP is more likely to cause severe pneumonia. It can damage the pulmonary tissue and seriously endanger the health of children. Clinical studies have confirmed that mixed-infected children with pneumonia have a longer course and are more likely to develop pulmonary lesions and pleural effusion. Among them, SP is the most common [6] and it is gradually being paid attention to in clinic. Thus, effective identification of MP infection and mixed infection of MP and streptococcus has vital reference significance for the treatment of childhood pneumonia. The imaging examination can be adopted to quickly observe the morphology and scope of the pulmonary lesions and know the effect of disease treatment and subsequent changes in the disease in order to provide a basis for treatment. Therefore, the most commonly applied technology for detecting pneumonia in children is imaging technology, including chest X-ray and CT.

The multislice spiral CT method is used with a scanning layer, and there are different conditions for scanning. Regular chest CT scans of children are done in calm breathing state. The underwent breathless scanning is held by the older children. The MP antibody is detected by the passive agglutination method (MP-IgM) with patient's serum twice every 10 or 14 days [7]. The two experienced radiologists assessed the CT imaging and retrospectively diagnosed the diseases including the lesion characteristics and lesions involving lobes. The ground glass opacity (GGO), the consolidation opacity, and the mass opacity are included by the lesion types. Peribronchovascular nodules

are presented in the bronchovascular bundle, and mildly increased attenuation without obscuration of the underlying vasculature is known as GGO [8, 9]. There are three types of nodules:

- (1) Centrilobular nodules in the centrilobular location
- (2) Peribronchovascular nodules in the bronchovascular bundles
- (3) Granulomas

Studies have shown that interstitial changes are the pathological basis of MPP [10]. It is the first to damage the body's terminal and respiratory bronchiolar epithelial cells, so as to cause the parabronchial tissues to infiltrate into the interlobular septum, thereby resulting in thickening of the interlobular septum and edema of the bronchiole wall. The lesions are mainly concentrated in the small and medium airways [11]. The cuffing signs and thickening of the bronchial wall can be observed in the thin-layer CT images of the chest, showing ring sign, orbit sign, and thickening of the bronchial vascular bundle [12]. If the condition is mild, the interlobular space will be thickened, and a small part of the pulmonary tissues will be also thickened. However, most will become asymmetric and irregular high-density small shadows. At this time, the lesions will merge with each other. The invasion function of bacterial capsule is the main therapeutic factor of SP. Invasion of tissues first causes edema of the alveolar wall, and then, white blood cells and red blood cells exudate. At this time, the alveoli are quickly and directly invaded by bacteria. The bacteria can even invade directly, causing symptoms such as congestion and edema in the pulmonary lobes.

Many researchers have worked on differential diagnosis of *Mycoplasma pneumoniae* pneumonia and *Mycoplasma pneumoniae* combined with streptococcal pneumonia in children for many years. The scientific basis for clinical diagnosis and severity assessment are provided for the improvement of comprehension of the imaging findings for the children chest imaging discussion. In the pediatric department, 126 cases of children are analyzed [13]. With chest computed tomography, this paper aims to clarify the abnormalities pattern with *Mycoplasma pneumoniae* pneumonia, and *M. pneumoniae* pneumonia from *Streptococcus pneumoniae* pneumonia is distinguished through the radiographic findings [14]. The CT case of different cases is performed by the retrospective review. The bilateral bronchial wall thickening or centrilobular nodules were seen in the patients. In the same patients, CT findings between early stage and progressed stage are compared and in the progressed stage, early stage radiographic features were not clearly observed. The wall thickening and centrilobular nodules in the CT outcomes are found by the *M. pneumoniae* pneumonia diagnosis. From the recent publications, the comprehensive radiological literature review is provided on ongoing radiological investigation of the imaging features of the chest ultrasound (US), radiographs (CXR), and computed tomography (CT) examinations. The evaluation and analysis of multimodality

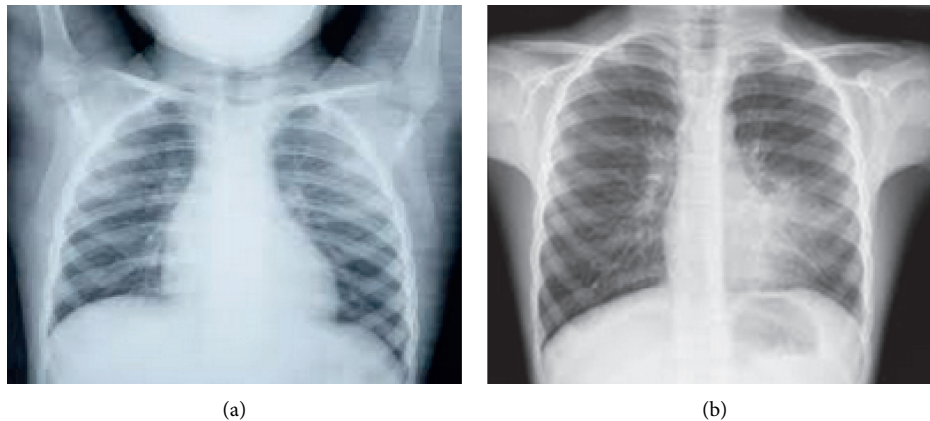


FIGURE 1: (a) Childhood pneumonia. (b) Fight against pneumonia.

imaging outcomes are done [15]. In many patients, the different tests like chest US, CXR, and CT were performed. The glenohumeral instability of patient's MRI is analyzed, and torn labrum diagnosis is determined which can be confirmed by the surgical exploration [16]. The correct labral tear diagnoses are 80% obtained after the analysis. A clinical, radiological, and histological entity is organizing pneumonia which is classified as interstitial lung disease [17]. The new understandings of the clinical and histological presentation are summarized in this work, and the most relevant CT features are reviewed. The author in this paper details many complications like pneumonia commonly accompanied by emphysema. The usual disease progression is changed by the destroyed airspaces [18]. Various cases of common comorbidities are demonstrated by the authors with unusual radiographic findings in emphysema patients. The proper management of emphysema patients is commonly diagnosed by the various emphysema findings. In this paper, the author details the radiographic findings which are nonspecific in mycoplasma pneumonia [19]. A single lobe is confined by the focal reticulonodular opacification which is radiographic pattern and closely associated with the mycoplasma infection. The mycoplasma pneumonia diagnosis is considered when bilateral reticulonodular opacification is seen. Due to confluent interstitial shadows, transient pseudoconsolidations are seen often. For the mycoplasma pneumonia diagnosis, radiographic findings are not sufficient. By combining the clinical findings, diagnosis accuracy is increased. The author describes the radiological features in adult patients with H1N1 influenza pneumonia [20]. During the epidemic of H1N1 influenza infection, descriptive study of retrospective data is performed. By RT-PCR, H1N1 influenza virus infection is confirmed by the 209 adult patients. The opacities were mainly bilateral, basal, and midzonal in CXR and peripheral in CT. In the H1N1 pneumonia, the predominant radiological pattern is bilateral and alveolar consolidation. To maximise iodine detection, preprocessing is done by the author in this paper for chest imaging in acute and chronic embolic diseases demonstration [21]. The work aims to set out the physical

basis for the technology and postprocessing protocols used and to present future developments.

The literature lacks the investigation of chest computed tomography (CT) findings of children patients with *Mycoplasma pneumoniae* pneumonia (MPP) and MP combined with streptococcal pneumonia (SP), which is very important. For the differential diagnosis references and treatment of MPP in clinic, reference is required. Clinically, the MP and SP mixed infection is very common, and the mixed pneumonia diagnosis is a critical research topic faced by pediatric respiratory physicians. In this paper, the main contribution of the work is to investigate the chest computed tomography (CT) findings of children patients with *Mycoplasma pneumoniae* pneumonia (MPP) and MP combined with streptococcal pneumonia (SP). In this study, 80 children patients with pneumonia were selected and were admitted to the Department of Respiratory Medicine of Indira Gandhi Medical Hospital from June 2019 to June 2020. Besides, 40 cases with MPP and 40 cases with MP combined with SP were enrolled into a MPP group and a MP + SP group in turn based on the results of serum MP-IgM detection and streptococcal blood culture. There were comparisons on the incidence of bronchial and pulmonary interstitial lesions, the degree of lymph node enlargement, the volume and depth of pleural effusion, and the location and morphology of the pulmonary lesions in the chest CT images of children patients from the two groups.

2. Materials and Methods

2.1. Clinical Research Objects. From June 2019 to June 2020, 80 children patients admitted to the Department of Respiratory Medicine of Indira Gandhi Medical Hospital for one year were selected as the research objects, who suffered from MMP and MP combined with SP confirmed by blood culture and serological examinations in turn. Among them, there were 40 cases in the MPP group, including 19 boys and 21 girls. Besides, they were 3–12 years old, with an average age of 7.50 ± 2.66 years [22–24]. There were also 40 cases in the MP + SP group (22 boys and 18 girls), with the age of 5–14 years (average age of 8.78 ± 2.99 years). The differences

in gender and age of the two groups were not statistically obvious ($P > 0.05$). All children patients underwent chest CT detections before receiving antibiotic treatment.

2.2. Operating Equipment and Methods. The children patients from the MPP group and the MP + SP group were given with chest CT scanning before treatment. The multislice spiral CT machine was adopted in this experiment [25]. What's more, they were asked to maintain breath-holding during the examination. The scanning range included chest cavity to lung base, with the adjustment of related parameters, and the corresponding data were uploaded to the workstation after scanning.

2.3. Observation Indicators. The 3 experienced imaging doctors examined all the research objects in this study and observed the CT images together in terms of the signs of bronchial and pulmonary interstitial lesions, the transverse diameter of lymph nodes and other specific manifestations, and the incidence and depth of pleural effusion. Then, the location and morphology of lesions in children patients from the two groups were analyzed based on the above observation indicators. According to these symptoms in children with pneumonia, the corresponding lesions might be judged [26, 27]. The lesion distribution presented on the CT images could be classified into consolidation, ground glass shadow, and reticular shadow on the basis of imaging density and divided according to lung lobes (anatomical unit) into left and right sides, and upper and lower lobes.

2.4. Statistical Methods. The measurement data were represented by mean \pm standard deviation ($\bar{x} \pm s$), and the disordered classification data were expressed as percentage (%). SPSS 20.0 software was employed to analyze the difference between the two groups [28]. Above all, $P > 0.05$ meant that the difference was not statistically substantial, and $P < 0.05$ indicated there was a statistically marked difference.

2.5. Clinical Features of Mycoplasma Infection. For mycoplasma pneumonia, humans are the only known reservoir. It is the tiny organism which is less than $350 \mu\text{m}$ and not visible at light microscopy [5]. This infection is spread by direct contact for the period of 1-2 weeks. It is an important cause of community-acquired respiratory infections in school-age children. Mycoplasma pneumonia illness is gradual, and its symptoms are nonspecific. The illness may begin in the upper respiratory tract and is often accompanied by low-grade fever, headache, and myalgias [29–32]. The rales, rhonchi, and decreased breath sounds are the different clinical signs included in the lungs mycoplasma infection. Usually the white blood cell count is in normal range. The respiratory symptoms precede the nonrespiratory manifestations in most of the cases, but there is little effect of pulmonary disease on subsequent neurologic disease [33].

3. Results and Discussion

3.1. Children with Bronchial and Interstitial Lung Disease from the Two Groups. The chest CT findings of bronchial and pulmonary interstitial lesions in children patients from the MPP group and MP + SP group were observed and compared, and the comparison results are shown in Table 1 and graphically shown in Figure 2. The CT images of children patients from the MPP group showed reticular shadows, ground glass shadows, reticular shadows, bronchial inflation phase, tube wall thickening, and vascular bundle thickening, and the appearance proportion of the above in the MPP group was higher obviously than that of the MP + SP group ($P = 0.03$ and $P < 0.05$) [34]. Besides, Figure 3 indicates the specific signs of chest CT in one child patient from the MPP group (the image of this patient was typical). The proportions of cases with bronchopulmonary emphysema and bronchial inflation phase from the two groups were compared, with no statistically obvious difference ($P = 0.94$ and $P > 0.05$).

3.2. Children with Pleural Effusion and Lymph Node Enlargement from the Two Groups. The largest transverse diameter of enlarged lymph nodes in the MPP group and the MP + SP group was $7.23 \pm 2.38 \text{ mm}$ and $9.68 \pm 2.95 \text{ mm}$, respectively. It was found that the transverse diameter of enlarged lymph nodes in children patients from the MP + SP group was greatly larger than that of the MPP group ($P = 0.04$ and $P < 0.05$) (Table 2). The depth of pleural effusion in children patients from the MPP group was $3.35 \pm 2.23 \text{ mm}$, while the depth of the MP + SP group was $12.75 \pm 11.36 \text{ mm}$ [35, 36]. Thus, the depth of pleural effusion in children patients from the MP + SP group rose hugely in contrast to the depth of the MPP group ($P = 0.009$ and $P < 0.05$). Figure 4 shows that the incidence of pleural effusion in children patients from the MPP group (22%) reduced steeply in contrast to the incidence of the MP + SP group (55%) ($P = 0.031$ and $P < 0.05$).

3.3. The Pathogenic Sites in the Lungs of the Sick Children. There was a comparison of the pathogenic sites of children patients from the MPP group and MP + SP group ($P > 0.05$), and the results are presented in Tables 3 and 4 and graphically shown in Figures 5 and 6 for better analysis and visualization.

3.4. Morphology of Pulmonary Lesions in Sick Children. In the MPP group, 33 cases had fan-shaped thin slice shadows in the lungs, and the incidence was 83%. Besides, there were 7 cases with fan-shaped thin slice shadows in the MP + SP group (18%). Thus, the above was statistically different ($P < 0.05$). As for irregular pulmonary consolidation, there were 36 in the MP + SP group (90%) and 9 in the MPP group (23%), and the difference was statistically substantial ($P < 0.05$) (Figure 7).

The results of this study revealed that the proportion of reticular shadow, ground glass shadow, bronchial inflation phase, tube wall thickening, and vascular bundle thickening in chest CT images of the MPP group was markedly higher than that of the MP + SP group. The damage of MPP was

TABLE 1: Chest CT findings and infection rate of bronchial and pulmonary interstitial lesions in children patients from the MPP group and MP + SP group (%).

| Chest CT findings | MPP group (n = 40) | | MP + SP group (n = 40) | |
|----------------------------|--------------------|--------------------|------------------------|--------------------|
| | Number of cases | Infection rate (%) | Number of cases | Infection rate (%) |
| Bronchopulmonary emphysema | 8 | 15 | 10 | 25 |
| Reticular shadow | 34 | 80 | 12 | 30 |
| Ground glass shadow | 24 | 60 | 7 | 18 |
| Bronchial inflation phase | 37 | 93 | 32 | 80 |
| Tube wall thickening | 38 | 95 | 20 | 50 |
| Vascular bundle thickening | 32 | 70 | 13 | 33 |

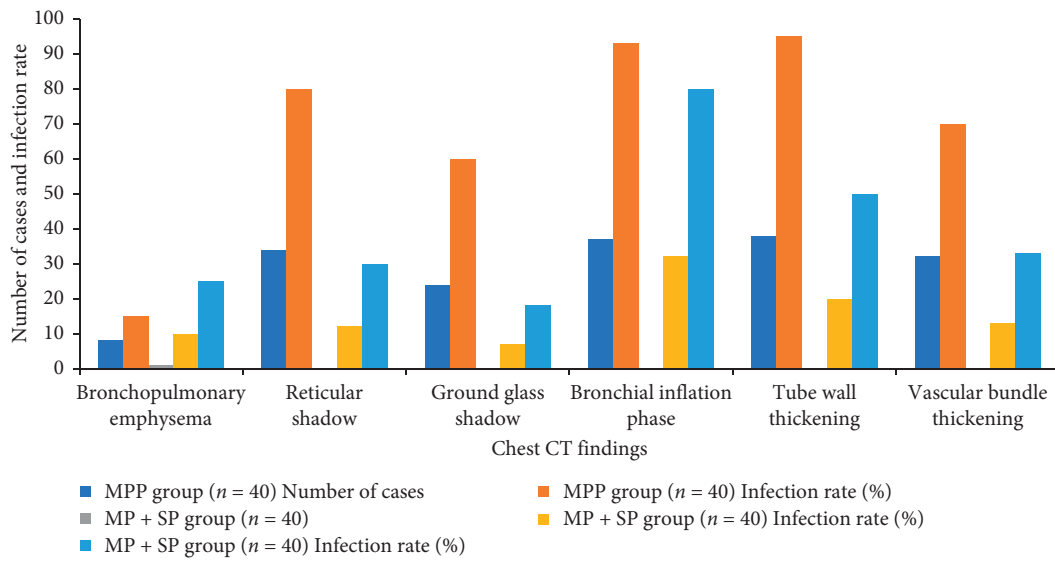


FIGURE 2: Chest CT findings and infection rate of bronchial and pulmonary interstitial lesions.



FIGURE 3: Chest CT image of one child patient from the MPP group.

TABLE 2: Comparison of the depth of pleural effusion and the maximum transverse diameter of lymph nodes in children patients from both groups ($\bar{x} \pm s$).

| Group | Depth of pleural effusion | Maximum transverse diameter of lymph nodes |
|------------------------|---------------------------|--|
| MPP group (n = 40) | 3.35 ± 2.23 | 7.23 ± 2.38 |
| MP + SP group (n = 40) | 12.75 ± 11.36 | 9.68 ± 2.95 |
| P value | <0.05 | <0.05 |

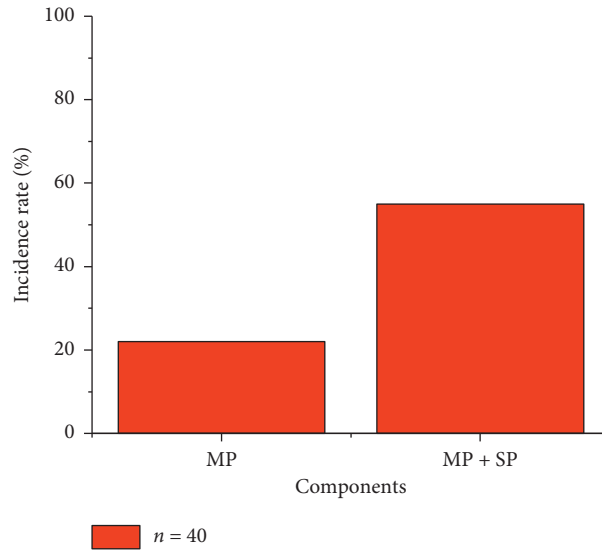


FIGURE 4: The incidence of pleural effusion in children patients from the two groups.

TABLE 3: Comparison of the left lung lesions of children patients from the two groups.

| Group | Number of cases | Left lung | | | |
|----------------|-----------------|-----------------|----|-----------------|----|
| | | Upper lobe | | Lower lobe | |
| | | Number of cases | % | Number of cases | % |
| MPP group | 40 | 20 | 50 | 14 | 35 |
| MP + SP group | 40 | 15 | 38 | 17 | 43 |
| <i>P</i> value | | >0.05 | | | |

TABLE 4: Comparison of the right lung lesion sites of children patients from the two groups.

| Group | Number of cases | Right lung | | | | | |
|----------------|-----------------|-----------------|----|-----------------|----|-----------------|----|
| | | Upper lobe | | Middle lobe | | Upper lobe | |
| | | Number of cases | % | Number of cases | % | Number of cases | % |
| MPP group | 40 | 10 | 25 | 14 | 35 | 11 | 28 |
| MP + SP group | 40 | 13 | 33 | 12 | 30 | 15 | 38 |
| <i>P</i> value | | >0.05 | | | | | |

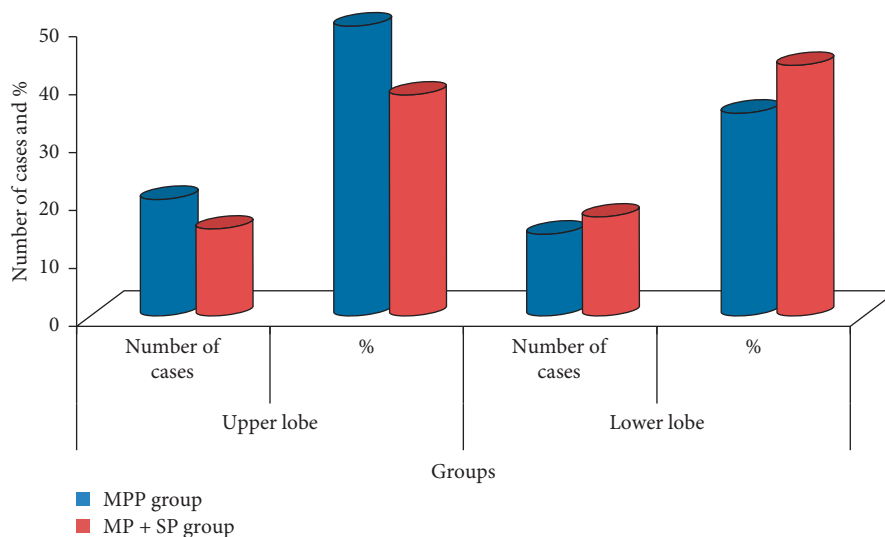


FIGURE 5: Left lung lesions of children patients from the two groups.

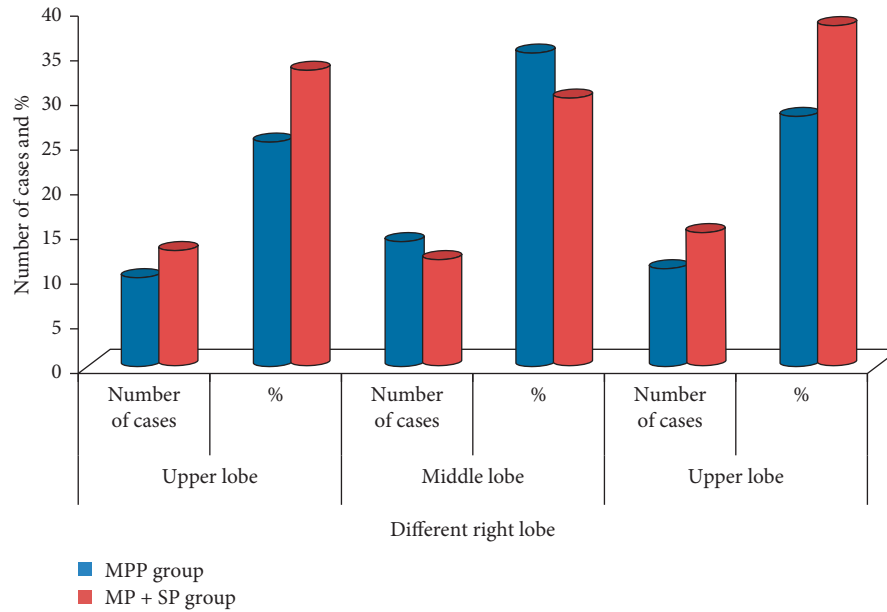


FIGURE 6: Right lung lesion sites of children patients from the two groups.

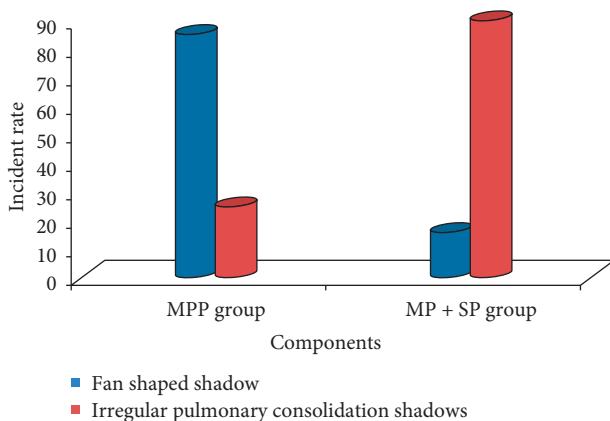


FIGURE 7: The incidence of two types of pulmonary lesions in children patients from the two groups.

most representative in the terminal and respiratory bronchiole epithelium, so the accumulation and infiltration of mononuclear lymphocytes will occur in some tissues clinically, and eventually the symptom of bronchopulmonary emphysema will appear. Therefore, thickening of the bronchial wall and the bronchial vascular bundle could be discovered on the chest CT images. With the progression of the disease, the surrounding tissues of the bronchiole would be infiltrated by inflammation again, so that the interlobular septa were thickened [37–39]. The alveolar cavity was the main site of SP inflammation, leading to the symptoms of pulmonary congestion and edema.

4. Discussion

The inflammatory response of MP combined with SP is more severe than that of MPP alone, and it is manifested as a more substantial local inflammatory exudation rate and

less air bubbles in the alveolar cavity. On the CT images, the translucency of the lung field was reduced [40–42]. However, a large area of dense shadows in the lungs could be observed on the CT images when a large amount of inflammatory exudation led to the loss of air in the alveoli, which could block the pulmonary interstitial changes caused by MPP [43]. Therefore, the proportion of ground glass shadow and reticular shadow in children patients from the MP + SP group decreased sharply. Studies have pointed out that hilar lymph node enlargement has occurred in about 1/5 of patients with pneumonia, most of which have been unilateral. Lymph node enlargement behind the anterior tracheal vena cava was observed in all children patients in this study, which was basically the same as the research results of relevant literature. In addition, the maximum transverse diameter of lymph node enlargement in children patients from the MPP group (7.23 ± 2.38 mm) dropped hugely compared with the MP + SP group (9.68 ± 2.95 mm). It indicated that children patients with obvious lymph node enlargement in the actual clinical setting had the possibility of mixed infection; for example, the maximum transverse diameter was more than 0.9 cm.

In this study, the incidence of pleural effusion in children patients from the MPP group was 22%, while the incidence of pleural effusion in the MP + SP group was 55%. Thus, the above incidence of the MP + SP group was dramatically higher than that of the MPP group, which was mainly caused by the inflammatory exudation after MP infection and the induced pleural response [44–46]. Inflammation can further enhance the permeability of the local capillary wall. At this time, the inflammatory exudate increases, thus making the pleural effusion obviously more. For all the children patients with pneumonia with relatively more pleural effusion, the possibility of suffering from MP combined with SP could not be excluded.

From the perspective of the pathogenesis of MPP and SP, there is little difference in the sites of the two types of pneumonia. It was consistent with the research of left and right pulmonary lesions in this study. Left lung lesions were slightly greater than right lung lesions, but there was no difference between the two types of pneumonia.

In this study, the irregular pulmonary consolidation shadows appeared in the CT images of 36 children patients from the MP + SP group, with an incidence of 90%, which was markedly higher than the incidence of the MPP group. There were consolidation shadows with irregular shapes after the onset of lesions, and this was because of the result of lesion fusion due to the inflammation of alveoli. It was also in line with the pathologic findings of MP combined with SP.

5. Conclusion

Pneumonia is the most frequent disease in children, and its main causes are pathogen infection and body allergic reactions. In the past 3 years, MPP has become a common pneumonia in children and adolescents, accounting for 10%–40% of community-acquired pneumonia, and its infection rate is 10%–20%. For the sake of medical ethics, the differences in the two types of pneumonia were observed on the basis of CT detection. However, there is a lack of comparison of the chest X-ray examinations of children patients from the two groups. The 3 experienced imaging doctors examined all the research objects in this study and observed the CT images together in terms of the signs of bronchial and pulmonary interstitial lesions, the transverse diameter of lymph nodes and other specific manifestations, and the incidence and depth of pleural effusion. Then, the location and morphology of lesions in children patients from the two groups were analyzed based on the above observation indicators. It is planned to carry out further comparison of the differential diagnosis between the two groups by chest X-ray examination, which may be more convincing and is better to expand the application of chest X-ray in the treatment of MPP and SP. The irregular pulmonary consolidation shadows appeared in the CT images of 36 children patients from the MP + SP group, with an incidence of 90%, which was markedly higher than the incidence of the MPP group; the alveolar inflammation could be observed on the CT images shown when children patients were combined with SP infection. The more obvious manifestations were that the flaky shadows appeared in the lungs, the pleural effusion became thicker, and the transverse diameters of enlarged lymph nodes were bigger. There were consolidation shadows with irregular shapes after the onset of lesions, and this was because of the result of lesion fusion due to the inflammation of alveoli. It was also in line with the pathologic findings of MP combined with SP. The investigation of the emerging COVID-19 pneumonia's imaging features on chest ultrasound (US) and computed tomography (CT) examinations can be focused on in the future research.

Data Availability

The data are available upon request to the corresponding author.

Conflicts of Interest

The authors have no conflicts of interest.

Acknowledgments

The authors acknowledge Indira Gandhi Medical Hospital for providing data.

References

- [1] W. S. Chen, H. H. Zhu, and G.-S. Feng, "Treating leukemia at the risk of inducing severe anemia," *Experimental Hematology*, vol. 44, no. 5, pp. 329–331, 2016.
- [2] M. Ohana, M. Y. Jeung, A. Labani, S. El Ghannudi, and C. Roy, "Thoracic dual energy CT: acquisition protocols, current applications and future developments; scanographie double energie en pathologie thoracique: protocoles d'exploration, applications actuelles et developpements," *Journal de Radiologie Diagnostique et Interventionnelle*, vol. 95, 2014.
- [3] J. K. Mansel, E. C. Rosenow, T. F. Smith, and J. W. Martin, "Mycoplasma pneumoniae pneumonia," *Chest*, vol. 95, no. 3, pp. 639–646, 1989.
- [4] C. Kang, Y. Vali, M. Naeem, and R. Reddy, "Cryptogenic organising pneumonia presenting with spontaneous pneumothorax and the value of procalcitonin: a case report," *Respiratory Medicine Case Reports*, vol. 22, pp. 36–38, 2017.
- [5] H. F. Zhang, H. T. Bai, J. M. Li, H. Xie, and Y. Wang, "Association of drug resistance of Mycoplasma pneumoniae with DNA load and genotypes in children with Mycoplasma pneumoniae pneumonia," *Zhongguo Dang Dai Er Ke Za Zhi*, vol. 19, no. 11, pp. 1180–1184, 2017.
- [6] C. H. Park, E. V. Valore, A. J. Waring, and T. Ganz, "Hepcidin, a urinary antimicrobial peptide synthesized in the liver," *Journal of Biological Chemistry*, vol. 276, no. 11, pp. 7806–7810, 2001.
- [7] Y. S. Youn, K. Y. Lee, J. Y. Hwang et al., "Difference of clinical features in childhood Mycoplasma pneumoniae pneumonia," *BMC Pediatrics*, vol. 10, no. 1, pp. 48–57, 2010.
- [8] Y.-S. Youn and K.-Y. Lee, "Mycoplasma pneumoniae pneumonia in children," *Korean Journal of Pediatrics*, vol. 55, no. 2, p. 42, 2012.
- [9] A. Sharma and R. Kumar, "Computation of the reliable and quickest data path for healthcare services by using service-level agreements and energy constraints," *Arabian Journal for Science and Engineering*, vol. 44, no. 11, pp. 9087–9104, 2019.
- [10] M. J. Søndergaard, M. B. Friis, D. S. Hansen, and I. M. Jørgensen, "Clinical manifestations in infants and children with Mycoplasma pneumoniae infection," *PLoS One*, vol. 13, no. 4, 2018.
- [11] T. Saraya, T. Watanabe, Y. Tsukahara et al., "The correlation between chest X-ray scores and the clinical findings in children and adults with mycoplasma pneumoniae pneumonia," *Internal Medicine*, vol. 56, no. 21, pp. 2845–2849, 2017.
- [12] Y.-l. Meng, W.-m. Wang, D.-d. Lv et al., "The effect of Platydocodin D on the expression of cytoadherence proteins P1 and P30 in Mycoplasma pneumoniae models," *Environmental Toxicology and Pharmacology*, vol. 49, pp. 188–193, 2017.
- [13] Z. Lyv, T. Chen, L. Mao et al., "The chest CT imaging characteristics of mycoplasma pneumoniae with different age groups of children," *Radiology of Infectious Diseases*, vol. 4, no. 4, pp. 150–156, 2017.







- [14] N. Miyashita, T. Sugiu, Y. Kawai et al., "Radiographic features of Mycoplasma pneumoniae pneumonia: differential diagnosis and performance timing," *BMC Medical Imaging*, vol. 9, no. 1, pp. 7-8, 2009.
- [15] P. Lomoro, F. Verde, F. Zerboni et al., "COVID-19 pneumonia manifestations at the admission on chest ultrasound, radiographs, and CT: single-center study and comprehensive radiologic literature review," *European Journal of Radiology Open*, vol. 7, Article ID 100231, 2020.
- [16] A. Bartolomé, T. Pirogova, M. J. Bartolomé, R. Sánchez, and F. García de Lucas, "Glenohumeral instability: validity of low-field MRI for diagnosis of labral tears," *The Egyptian Journal of Radiology and Nuclear Medicine*, vol. 47, no. 4, pp. 1521-1528, 2016.
- [17] M. Baque-Juston, A. Pellegrin, S. Leroy, C. H. Marquette, and B. Padovani, "Organizing pneumonia: what is it? a conceptual approach and pictorial review," *Diagnostic and Interventional Imaging*, vol. 95, no. 9, pp. 771-777, 2014.
- [18] J. H. Baik, J. M. Ko, and H. J. Park, "Pitfalls in radiographic interpretation of emphysema patients," *Canadian Association of Radiologists Journal*, vol. 67, no. 3, pp. 277-283, 2016.
- [19] S. D. John, J. Ramanathan, and L. E. Swischuk, "Spectrum of clinical and radiographic findings in pediatric mycoplasma pneumonia," *Radiographics*, vol. 21, no. 1, pp. 121-131, 2001.
- [20] M. Abdelsalam, H. S. Diab, and Y. Ragab, "Radiological findings in patients with H1N1 influenza pneumonia," *Egyptian Journal of Chest Diseases and Tuberculosis*, vol. 65, no. 1, pp. 135-142, 2016.
- [21] M. Ohana, M. Y. Jeung, A. Labani, S. El Ghannudi, and C. Roy, "Thoracic dual energy CT: acquisition protocols, current applications and future developments," *Diagnostic and Interventional Imaging*, vol. 95, no. 11, pp. 1017-1026, 2014.
- [22] Z. Luo, J. Luo, E. Liu et al., "Effects of prednisolone on refractory mycoplasma pneumoniae pneumonia in children," *Pediatric Pulmonology*, vol. 49, no. 4, pp. 377-380, 2014.
- [23] B. Medjo, M. Atanaskovic-Markovic, S. Radic, D. Nikolic, M. Lukac, and S. Djukic, "Mycoplasma pneumoniae as a causative agent of community-acquired pneumonia in children: clinical features and laboratory diagnosis," *Italian Journal of Pediatrics*, vol. 40, no. 1, pp. 104-107, 2014.
- [24] D. Kumar, A. Sharma, R. Kumar, and N. Sharma, "Restoration of the network for next generation (5G) optical communication network," in *Proceedings of the 2019 International Conference on Signal Processing and Communication (ICSC)*, pp. 64-68, Noida, India, March 2019.
- [25] M. Poongodi, A. Sharma, V. Vijayakumar et al., "Prediction of the price of Ethereum blockchain cryptocurrency in an industrial finance system," *Computers & Electrical Engineering*, vol. 81, 2020.
- [26] G. H. Mccracken Jr., "Diagnosis and management of pneumonia in children," *The Pediatric Infectious Disease Journal*, vol. 19, no. 9, pp. 924-928.
- [27] T. Q. Tan, E. O. Mason, E. R. Wald et al., "Clinical characteristics of children with complicated pneumonia caused by Streptococcus pneumoniae," *Pediatrics*, vol. 110, no. 1, pp. 1-6, 2002.
- [28] B. Lassmann, M. Poetschke, P. Apfalter et al., "Community-acquired pneumonia in children in Lambarene, Gabon," *The American Journal of Tropical Medicine and Hygiene*, vol. 79, no. 1, pp. 109-114, 2008.
- [29] A. B. Cengiz, G. Kanra, M. Çağlar, A. Kara, S. Güçer, and T. Ince, "Fatal necrotizing pneumonia caused by group A streptococcus," *Journal of Paediatrics and Child Health*, vol. 40, no. 1, pp. 69-71, 2004.
- [30] M. P. Muller, D. E. Low, K. A. Green et al., "Clinical and epidemiologic features of group A streptococcal pneumonia in Ontario, Canada," *Archives of Internal Medicine*, vol. 163, no. 4, pp. 467-472, 2003.
- [31] O. Wisesa, A. Adriansyah, and O. I. Khalaf, "Prediction analysis sales for corporate services telecommunications company using Gradient boost algorithm," in *Proceedings of the 2nd International Conference on Broadband Communications, Wireless Sensors and Powering (BCWSP)*, pp. 101-106, Yogyakarta, Indonesia, September 2020.
- [32] A. F. Subahi, Y. Alotaibi, O. I. Khalaf, and F. Ajesh, "Packet drop battling mechanism for energy aware detection in wireless networks," *Computers, Materials and Continua*, vol. 66, no. 2, pp. 2077-2086, 2020.
- [33] X. Xiang, Q. Li, S. Khan, and O. I. Khalaf, "Urban water resource management for sustainable environment planning using artificial intelligence techniques," *Environmental Impact Assessment Review*, vol. 86, Article ID 106515, 2021.
- [34] J. L. Basiliere, H. W. Bistrong, and W. F. Spence, "Streptococcal pneumonia," *The American Journal of Medicine*, vol. 44, no. 4, pp. 580-589, 1968.
- [35] K. Mleczko-Sanecka, G. Casanovas, A. Ragab et al., "SMAD7 controls iron metabolism as a potent inhibitor of hepcidin expression," *Blood*, vol. 115, no. 13, pp. 2657-2665, 2010.
- [36] P.-P. Cheng, Z.-Z. Sun, F. Jiang, Y.-T. Tang, and X.-Y. Jiao, "Hepcidin expression in patients with acute leukaemia," *European Journal of Clinical Investigation*, vol. 42, no. 5, pp. 517-525, 2012.
- [37] A. C. Nascimento-Carvalho, O. Ruuskanen, and C. M. Nascimento-Carvalho, "Comparison of the frequency of bacterial and viral infections among children with community-acquired pneumonia hospitalized across distinct severity categories: a prospective cross-sectional study," *BMC Pediatrics*, vol. 16, no. 1, p. 105, 2016.
- [38] M. Krichen, S. Mechti, R. Alrobaea et al., "A formal testing model for operating room control system using internet of things," *Computers, Materials & Continua*, vol. 66, no. 3, pp. 2997-3011, 2021.
- [39] O. I. Khalaf, K. A. Ogudo, and M. Singh, "A fuzzy-based optimization technique for the energy and spectrum efficiencies trade-off in cognitive radio-enabled 5G network," *Symmetry*, vol. 13, no. 1, p. 47, 2021.
- [40] O. I. Khalaf, F. Ajesh, A. A. Hamad, G. N. Nguyen, and D.-N. Le, "Efficient dual-cooperative bait detection scheme for collaborative attackers on mobile ad-hoc networks," *IEEE Access*, vol. 8, pp. 227962-227969, 2020.
- [41] A. A. Hamad, A. S. Al-Obeidi, E. H. Al-Taiy, O. Ibrahim Khalaf, and D.-N. Le, "Synchronization phenomena investigation of a new nonlinear dynamical system 4-D by Gardano's and Lyapunov's methods," *Computers, Materials & Continua*, vol. 66, no. 3, pp. 3311-3327, 2021.
- [42] O. I. Khalaf and G. M. Abdulsahib, "Energy efficient routing and reliable data transmission protocol in WSN," *International Journal of Advances in Soft Computing and its Application*, vol. 12, pp. 345-353, 2020.
- [43] O. I. Khalaf, G. M. Abdulsahib, and B. M. Sabbar, "Optimization of wireless sensor network coverage using the Bee algorithm," *Journal of Information Science and Engineering*, vol. 36, no. 2, pp. 377-386, 2020.
- [44] S. K. Prasad, J. Rachna, O. I. Khalaf, and D.-N. Le, "Map matching algorithm: real time location tracking for smart security application," *Telecommunications and Radio Engineering*, vol. 79, no. 13, pp. 1189-1203, 2020.
- [45] S. A. Rhedin, A. Eklundh, M. Ryd-Rinder et al., "Introducing a new algorithm for classification of etiology in studies on

pediatric pneumonia: protocol for the trial of respiratory infections in children for enhanced diagnostics study,” *JMIR Research Protocols*, vol. 8, no. 4, Article ID e12705, 2019.

- [46] H. N. Njuguna, S. R. Zaki, D. J. Roberts et al., “Determining the cause of death among children hospitalized with respiratory illness in Kenya: protocol for pediatric respiratory etiology surveillance study (PRESS),” *JMIR Research Protocols*, vol. 8, no. 1, Article ID e10854, 2019.

Research Article

Boosting Breast Cancer Detection Using Convolutional Neural Network

Saad Awadh Alanazi ¹, M. M. Kamruzzaman ¹, Md Nazirul Islam Sarker ²,
Madallah Alruwaili ³, Yousef Alhwaiti ¹, Nasser Alshammari ¹,
and Muhammad Hameed Siddiqi¹

¹Department of Computer Science, College of Computer and Information Sciences, Jouf University, Sakakah, Saudi Arabia

²School of Political Science and Public Administration, Neijiang Normal University, Neijiang, China

³Department of Computer Engineering and Networks, College of Computer and Information Sciences, Jouf University, Sakakah, Saudi Arabia

Correspondence should be addressed to M. M. Kamruzzaman; mmkamruzzaman@ju.edu.sa

Received 18 January 2021; Revised 21 February 2021; Accepted 24 March 2021; Published 5 April 2021

Academic Editor: Anupam Kumar Bairagi

Copyright © 2021 Saad Awadh Alanazi et al. This is an open access article distributed under the Creative Commons Attribution License, which permits unrestricted use, distribution, and reproduction in any medium, provided the original work is properly cited.

Breast cancer forms in breast cells and is considered as a very common type of cancer in women. Breast cancer is also a very life-threatening disease of women after lung cancer. A convolutional neural network (CNN) method is proposed in this study to boost the automatic identification of breast cancer by analyzing hostile ductal carcinoma tissue zones in whole-slide images (WSIs). The paper investigates the proposed system that uses various convolutional neural network (CNN) architectures to automatically detect breast cancer, comparing the results with those from machine learning (ML) algorithms. All architectures were guided by a big dataset of about 275,000, 50 × 50-pixel RGB image patches. Validation tests were done for quantitative results using the performance measures for every methodology. The proposed system is found to be successful, achieving results with 87% accuracy, which could reduce human mistakes in the diagnosis process. Moreover, our proposed system achieves accuracy higher than the 78% accuracy of machine learning (ML) algorithms. The proposed system therefore improves accuracy by 9% above results from machine learning (ML) algorithms.

1. Introduction

Breast cancer forms in breast cells and is considered as a very common type of cancer in women. Breast cancer is also a very life-threatening disease of women after lung cancer. Breast cancer is categorized into various types according to the cell's appearance through a microscope. The two main types of breast cancer are (1) invasive ductal carcinoma (IDC) and (2) ductal carcinoma in situ (DCIS), with the latter evolving slowly and, generally, not having negative effects on the daily lives of patients. A low percentage of all cases (between 20% and 53%) are classified as the DCIS type; on the other hand, the IDC type is more dangerous, surrounding the entire breast tissue. Most breast cancer patients, approximately 80%, are in this category [1].

Breast cancer can be effectively treated through its early detection. Thus, the availability of proper screening methods is important for detecting the initial symptom of breast cancer. Various imaging techniques are used for the screening to identify this disease; the popular approaches are mammography, ultrasound, and thermography. One of the most significant methods of early detection for breast cancer is mammography. Ultrasound or diagnostic sonography methods are popularly used as mammography is not effective for solid breasts. Considering these issues, small masses can be bypassed by radiations from radiography and thermography may be more effective than the ultrasound technique in diagnosing smaller cancerous masses [2].

Due to the intrinsic difficulties associated with an image, with meagre contrast, noise, and lack of appreciation by the

eye, instruments have been prepared to make and improve image processing. Nowadays, artificial intelligence (AI), machine learning (ML), and convolutional neural network (CNN) are the quickest rising areas of healthcare industry [1, 3–6]. AI and ML are found in the research arena that deals with and improves technological systems to resolve complex tasks through reducing necessity of human intelligence [7–9].

Deep learning (DL) which is part of machine learning family depended on artificial neural networks. DL architectures, such as DNN (deep neural networks), RNN (recurrent neural networks), DBN (deep belief networks), and CNN, are generally applied to the areas like computer vision, audio recognition, speech recognition, social network filtering, natural language processing, machine translation, drug design, bioinformatics, medical image analysis, materials scrutiny, histopathological diagnosis, and board game programs [10–12]. These new technologies, in particular DL algorithms, can be applied to improve the diagnostic accuracy and efficiency of cancer detection [13].

On the other hand, digital pathology (DP) is a way of digitalization of histology slides for producing high-resolution images. These digitized images are used for detection, segmentation, and classification through the application of image analysis techniques. Extra steps are required in deep learning (DL) using CNNs, such as digital staining, to understand patterns for image classification [14].

The opportunity that CNN brings to research on medical imaging is not restricted to deep CNN for extraction of the imaging feature. Indeed, a second field that can support medical research is the use of CNN for synthetic image rendering. Wahab and Khan [15] conducted a study by using MF-CNN (multifaceted fused-CNN) and a hybrid descriptor and revealed that, to assist with mitotic count-based selection of ROIs at lower resolution, acceptable color and textural characteristics are established. The MF-CNN recognizes several facets of the input picture to acknowledge dynamic patterns. It includes mitoses, excerpts, and handmade features from ROIs and uses the global image texture to shape a hybrid descriptor to train a classifier assigning WSIs scores. CNNs are opening up to unimaginable scenarios in areas where it is tedious for domain experts to develop successful features. Gravina et al. [16] noted that the naive use of CNNs might not be successful, since “medical images are more exceptional than normal images.” Mammographic lesion segmentation has been shown to be an effective source of knowledge, as it may help both extract shape-related structures and provide exact lesion localization.

An experiment was performed by Tsochatzidis et al. [17] to test the diagnosis of breast cancer with mammograms using CNN. They show that performance assessment in diagnosis is carried out on two datasets of mammographic mass such as DDSM-400 and CBIS-DDSM, with variations in the accuracy of the corresponding segmentation maps of ground truth. A computer-aided diagnosis (CAD) system was applied by Malathi et al. [18] for mammograms to allow initial identification, examination, and treatment of breast cancer. They discussed exploring a breast CAD architecture focused on characteristic fusion through deep learning of the

CNN. The result reveals that the RFA (random forest algorithm) has the highest precision with less error than the CNN classifier (95.65 percent). The abnormality of the representations of the breast is investigated via the deep belief network (DBN). To discern the abnormal picture, the given work practices activate the contour segmentation and it may be ordered by the DBN. Desai and Shah [19] mentioned that deep comparison of the operation and architecture of each network is carried out and examination is then conducted based on the precision of the network's diagnosis and categorization of breast malignancy to assess which network outperforms the other. For the diagnosis and identification of breast cancer, CNN is observed to provide somewhat higher precision than MLP.

In prior research, Wahab and Khan [15] used CNNs to investigate the automated detection of IDC-type breast cancer. Several scholars used ML-based automatic detection techniques to detect the same. This aimed to obtain correct results to lessen the errors found in the diagnosis procedure. The study of Abdelhafiz et al. [20] also discovered that augmentation approach was fruitful in the automatic identification of this cancer, when using the given dataset. Another researcher [21] applied deep max pooling CNNs to identify images of mitosis in breast histology. The networks were competent to order the images based on pixel. A DL approach was used by Murtaza et al. [22] for the automatic identification and investigation of IDC tissue zones. Context-aware stacked CNNs were presented by Hossain [4] for the categorization of breast WSIs into simple, DCIS (ductal carcinoma in situ), and IDC (invasive ductal carcinoma). The system realized an area beneath the curve of 0.962 for the categorization of malignant and nonmalignant slides and obtained a three-class accurateness of 81.3% for WSI classification, demonstrating its potential for routine diagnostics. The works of Alhamid et al. [23] and Qian et al. [24] also presented some techniques to identify them. Their experiment results showed that the shearlet coefficients' magnitude and phase could enhance detection accuracy and generalizability.

Several previous studies have proposed using AI as well as CNN for image detection and healthcare monitoring [1, 18, 20, 25, 29]. But, for a medical side solution, which is around 60 percent for all class detection, 75 percent for only mass class, and 100 percent for only calcification, the accuracy percentage is too poor [26]. With the exception of only calcification argument, the accuracy of all argument and mass only argument can be further enhanced to obtain a better result [27]. Therefore, this research aims to increase precision level of breast cancer diagnosis using CNN. The current study proposes a system of breast cancer detection using several regression and DL techniques. The proposed system investigates several CNN architectures for the automatic detection of this type cancer. The proposed system initially uses a basic CNN and then adds it to three various architectures, all of which were guided by a big dataset of about 275,000, 50×50 -pixel RGB image patches. The quantitative findings will be measured by validation tests. The two main objectives of this current research are, firstly, to present an automated tool for detecting IDC to lessen human mistakes in the process of diagnosis and, secondly, to

examine the consequence of different types of CNN architecture in the proposed system. The remainder of this paper is organized as follows: The second section deals with materials and methods, the third section describes the results and discussions, and the final section deals with conclusion including recommendation, limitations, and future research.

2. Materials and Methods

2.1. Dataset. The dataset, Kaggle 162 H&E, was used for the proposed system [28]. Kaggle 162 H&E was also used by many researchers for similar kind of study [26, 30]. The data set consists of both benign and malignant images. Careful observation was ensured during splitting; the dataset was divided into validation data and testing data belonging to same distribution to well represent the model's generalized results. For learning indicators like weights and biases, training data is important, while validating data is essential for model verification and how exactly the model simplifies, thus tuning hyperparameters like learning rate and decay to boost the result of the model. A model's final output comes from precise work on the test results. To hold each pixel in the same range and prevent bias, the normalization has to be done on the whole image. Around 277,524 50×50 -pixel RGB digital image patches were extracted from 162 WSI mounts scanned samples. All patches were labelled as 1 (IDC positive) or 0 (IDC negative). Figure 1 presents examples of positive and negative tissues.

2.2. Data Process. All the patches are in RGB pixel format and are scaled from 0 to 255. We intended to apply machine learning (ML) classification methods to these images. Therefore, we made the scale between 0 and 1 to be compatible with the methods.

2.3. Machine Learning and Deep Learning to Predict Invasive Cancer. In this section, the proposed system is compared to the classic regression techniques and deep learning (DL), with these techniques explained in detail.

2.4. Machine Learning Classification Methods for Predicting Invasive Cancer. Classification in ML and statistics is a supervised learning method in which program learns from the given data and then uses it to classify new observations. The dataset is only allowed to be biclass or multiclass [31]. Speech recognition, document classification, biometric identification, handwriting recognition, and so forth are only a few significant examples of classification problems. The proposed system uses the following machine learning (ML) classifiers:

- (1) Logistic regression
- (2) K -nearest neighbor
- (3) Support vector machines

2.4.1. Logistic Regression (LR). Logistic regression is an estimation applied to forecast a binary outcome like either something happens or not. This may be shown as "Yes/No," "Pass/Fail," "Alive/Dead," and so forth. If we consider IDC (+) as 1 and IDC (−) as 0, then the output will be a categorical 0 or 1, which could be defined as

$$P(Y = 1|X) \quad (1)$$

or $P(Y = 0|X)$.

This estimates the likelihood of dependent variable Y , given independent variable X . The decision boundary of logistic regression can be linear or nonlinear, with an increase in the polynomial order resulting in a complex system. The cost function cannot be an R -squared function due to its nonconvex structure. Owing to the nature of the cost function in logistic regression (which includes Bernoulli distribution), the dependent variable also follows the same distribution, with this shown in Figure 2.

2.4.2. K -Nearest Neighbour (K -NN). K -nearest neighbor (k -NN) is an algorithm for pattern recognition which applies training datasets to explore the closest relatives to k in future examples. The theory for the nearest-neighbor algorithm is used to define several training samples adjoining to the new point and to use them to forecast the label.

The sample number may be a constant defined by the user, k -nearest neighbor (k -NN) learning, or may vary according to the local point density. The distance may be any metric measure: standard Euclidean distance is generally a common choice. The nearest neighbor is also available for a large number of datasets due to its simple structure, which can achieve better results for complex boundaries. In Figure 3, the larger values of K seem to have a smoother boundary with lower variances.

Euclidean distance is given by

$$d(x, y) = \sqrt{\sum_{i=1}^d (x_i - y_i)^2}, \quad (2)$$

for the vector $\mathbf{x} = (x_1, \dots, x_d)$ has d scalar components.

2.4.3. Support Vector Machines (SVM). It is effective in high-dimensional spaces. In an n -dimensional space, each data item is plotted as a point by this algorithm, where n denotes the feature number and each feature value indicates a unique coordinate value. It is then possible to carry out classification after getting the hyperplane that best differentiates the two classes, as shown in Figure 4.

2.5. Metrics. For the evaluation of machine learning classification models, accuracy is one metric. Accuracy is specified as the percentage of correct predictions for a model. Usually, accuracy is calculated with the following:

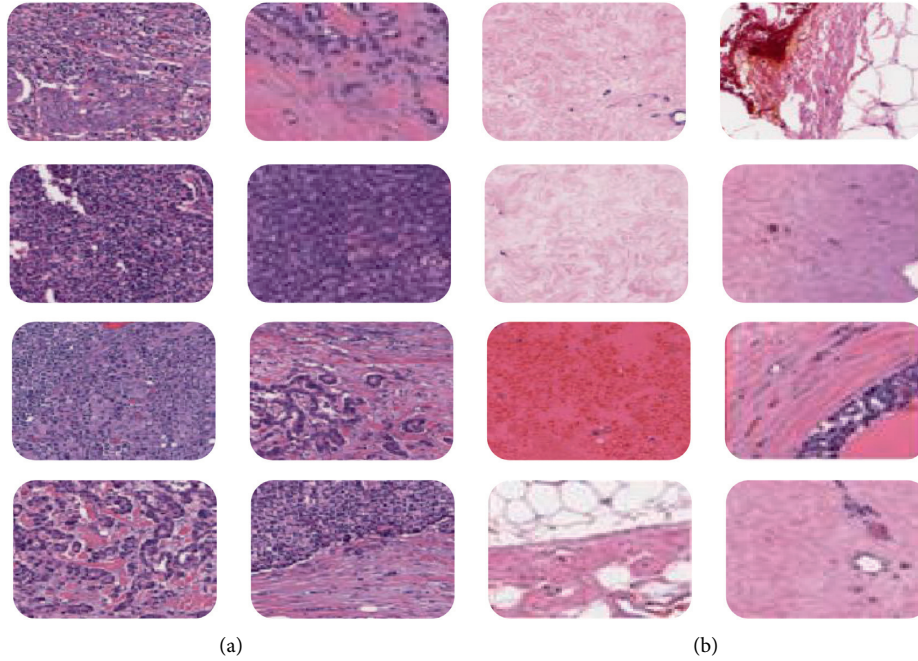


FIGURE 1: Tissue examples of IDC (+) and IDC (-). (a) IDC (+) tissue and (b) IDC (-) tissue.

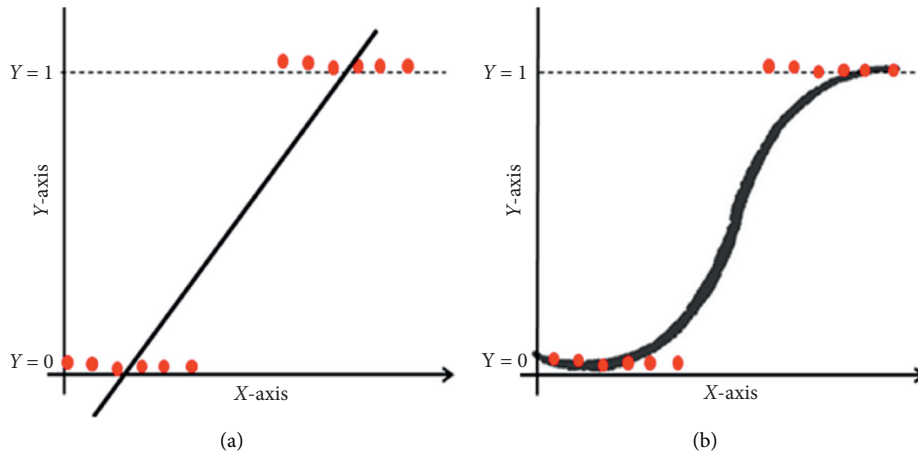


FIGURE 2: Linear regression (a) and logistic regression (b).

$$\text{accuracy} = \frac{\text{number of correct predictions}}{\text{total number of predictions}}. \quad (3)$$

Accuracy can also be evaluated as positive and negative for binary classification as follows:

$$\text{accuracy} = \frac{\text{TP} + \text{TN}}{\text{TP} + \text{TN} + \text{FP} + \text{FN}}, \quad (4)$$

where TP is used to represent True Positives, TN is used to represent True Negatives, FP is used to represent False Positives, and FN is used to represent False Negatives.

The true positives number divided by the true positives number plus the false positives number is known as precision as shown below:

$$\text{precision} = \frac{\text{TP}}{\text{TP} + \text{FP}}. \quad (5)$$

2.6. Deep Learning. Deep neural networks usually have several hidden layers in between input layer and output layer. These networks are used to retrieve features from images, unlike traditional ML algorithms which use hand-engineering features for breast cancer detection [32]. A new type of deep learning (DL) is machine learning neural networks (ML-NNs), with ML-NN structures mostly requiring a training stage to find optimum weights. The most frequently used learning rule is the backpropagation algorithm in which weights are updated systematically for every

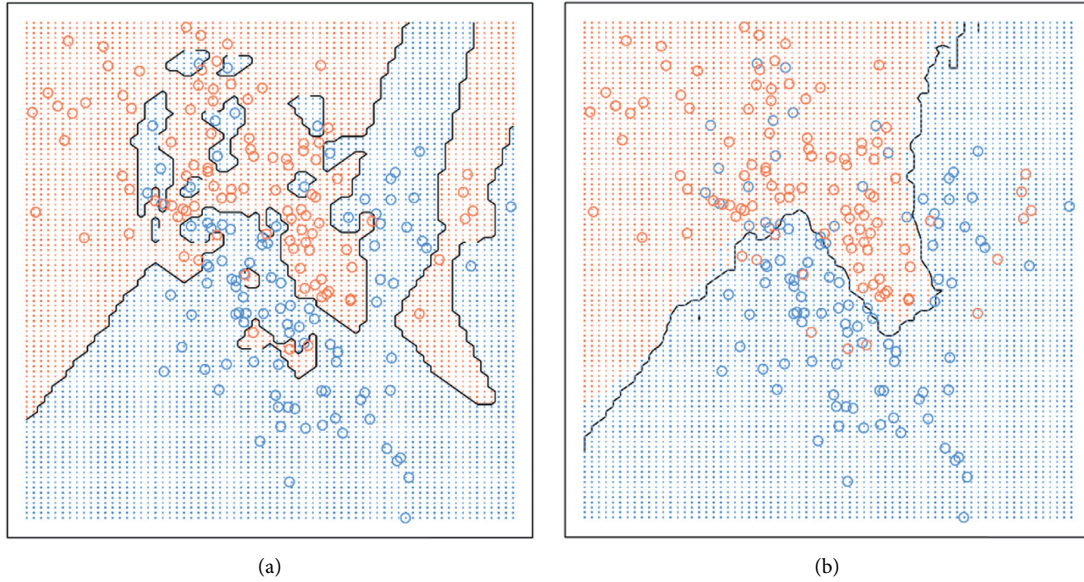


FIGURE 3: $K=1$ (a) and $K=20$ (b) for k -nearest neighbour boundaries.

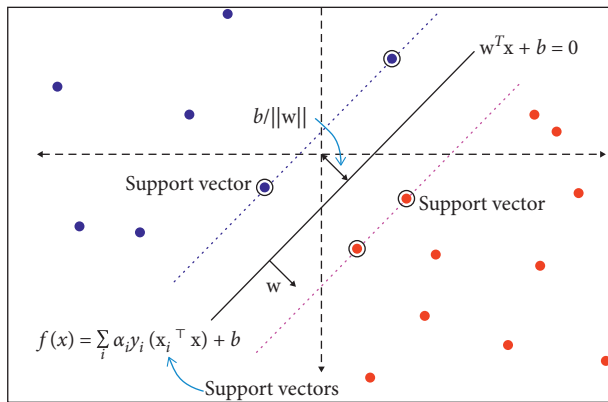


FIGURE 4: SVM formula.

pass depending upon the error rate obtained from the production layer with the gradient and chain rule.

2.7. Convolutional Neural Networks (CNNs). CNNs are applied to explore patterns in an image. This is done by convoluting over an image and looking for patterns [27]. The network can detect lines and corners in the few front layers of CNNs. Via our neural net, however, we can then transfer these patterns down and begin to identify more complex characteristics as we get deeper. This property ensures that CNNs are very effective at detecting objects in images [26]. The proposed system uses CNNs to detect breast cancer from breast tissue images.

The architecture of a CNN has 3 main layers, the convolutional layer, pooling layer, and fully connected layer, as shown in Figure 5. The first layer calculates the output of neurons which are linked with local regions. Each one is calculated by a dot product of weights and the region. For image inputs, typical filters are small in area such as 3×3 , 5×5 , or 8×8 . These filters scan the image by a sliding

window on the image, while learning the recurrent patterns which arise in any area of the image. The interval between filters is known as the stride. The convolution is extended to overlapping windows if the stride hyperparameter is smaller than the filter dimension. A detailed visual explanation of neural networks (NNs) is shown in Figure 6.

2.8. Pooling Layer. Convolutional layers bring out the features of images with precise positions. If the positions change, even a small amount for any reason, the feature maps will be different. To overcome this problem, the downsampling process must be done at the output of every convolutional layer [18]. With convolutional layers, downsampling can be done by changing the convolution's phase across the image. A more acceptable and common method is to use a pooling layer [33]. Using this process, outputs will be more accurate.

2.9. Dataset Augmentation Technique. Data augmentation is an effective and widely used tool to avoid the overfitting problem by creating additional data [34]. More complex systems using deep neural network have low bias but generate high variance. It means that these systems overfit the training data and will demonstrate bad performance on test data or on data that had not seen before. It would result in greater errors in prediction [19]. Therefore, the increased diversity from data augmentation decreases the model's variance by improving it at generalizing. The proposed system uses Gaussian Mixture Models (GMMs) for modeling and classification [35].

3. Results and Discussion

We have used scikit-learn machine learning framework for implementation in Python. Scikit-learn is most popular among data scientists. Also, there are other prerequisites to

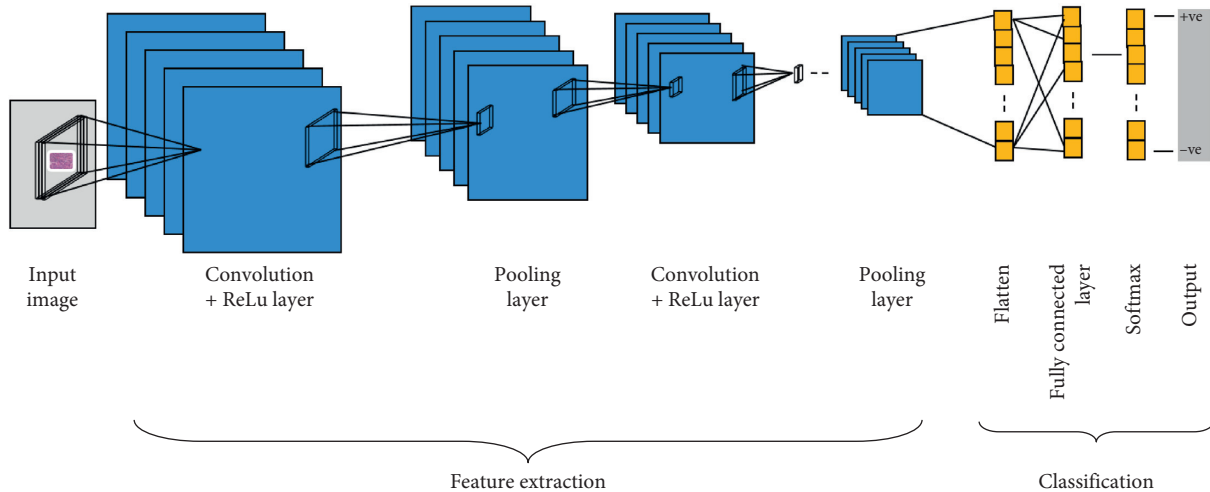


FIGURE 5: Typical CNN architecture for automatic detection of IDC breast cancer.

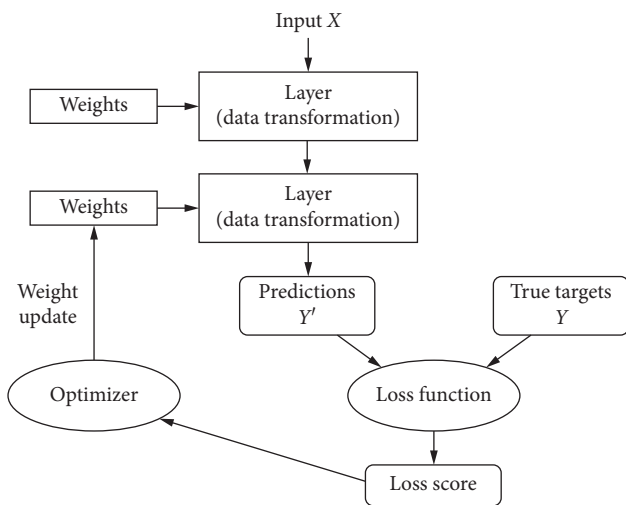


FIGURE 6: Detailed process of a neural network (NN).

run scikit-learn functions such as pandas, NumPy, matplotlib, and seaborn frameworks which have been used to implement the proposed system.

3.1. Predicting Invasive Cancer Using Machine Learning Classifiers. Table 1 presents the accuracies of machine learning (ML) classifiers. The highest level of accuracy is found in SVMs when compared to logistic regression (LR) and k -NN, as shown in Figure 7.

3.2. Predicting Invasive Cancer Using CNN Model 1. CNN Model 1 has two convolution layers with 32 and 64 kernels, which are checked with a dropout regularization of 25% to cancel overfitting. The image is then vectorized with a flattened layer for the next dense layer. The rectified linear unit (ReLU) is an activation function that is used in all layers with the exception of the output layer, for which the Softmax activation function is used [1].

TABLE 1: Standard machine learning classifiers.

| Classifier | Accuracy |
|------------|----------|
| LR | 0.7180 |
| KNN | 0.7126 |
| SVM | 0.7856 |

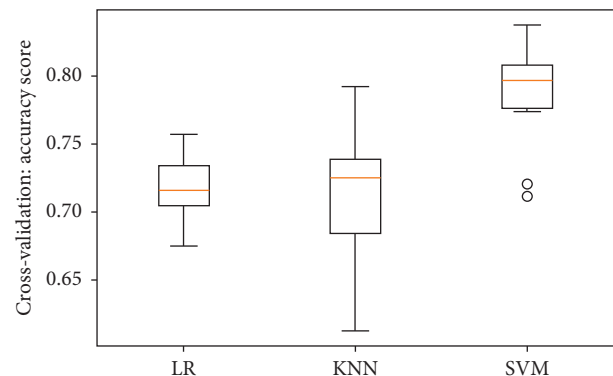


FIGURE 7: Algorithm comparison on accuracy.

This model has been trained with 12 epochs and the batch size is 128. The training loss is 0.69, while the validation is 0.68. Little difference is found between model's performances in the training set and the validation set [30]. Table 2 shows the configuration summary of Model 1 with the metrics results presented in Figure 8. It has 59% accuracy, which is less than standard machine learning (ML) classifiers, as shown in Table 3. The loss learning curve is shown in Figure 9.

3.3. Predicting Invasive Cancer Using CNN Model 2. To increase the number of features, convolution layers are tripled here [36]. The accuracy of the proposed system is thus increased to 0.76 as shown in Table 4, an improvement on Model 1. Table 5 shows the configuration summary of Model 2. The confusion matrix and the loss learning curve are

TABLE 2: The summary table of CNN Model 1.

| Layer | Type | Output shape | Param. |
|-----------------------------|--------------|------------------|---------|
| conv2d_2 | Conv2D | None, 48, 48, 32 | 896 |
| conv2d_1 | Conv2D | None, 46, 46, 64 | 18496 |
| max_pooling2d | MaxPooling2D | None, 23, 23, 64 | 0 |
| Dropout | Dropout | None, 23, 23, 64 | 0 |
| Flatten | Flatten | None, 33856 | 0 |
| Dense | Dense | None, 128 | 4333696 |
| dropout_1 | Dropout | None, 128 | 0 |
| dense_1 | Dense | None, 2 | 258 |
| Total params: 4,353,346 | | | |
| Trainable params: 4,353,346 | | | |
| Nontrainable params: 0 | | | |

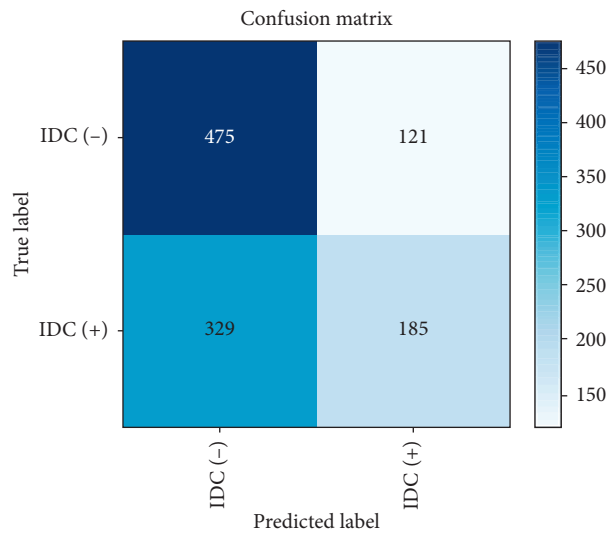


FIGURE 8: The confusion matrix of CNN Model 1.

TABLE 3: The metric results of CNN Model 1.

| | Precision | Recall | F1-score | Support |
|----------|-----------|--------|----------|---------|
| IDC (-) | 0.59 | 0.80 | 0.68 | 596 |
| IDC (+) | 0.60 | 0.36 | 0.45 | 514 |
| Accuracy | | | 0.59 | 1110 |

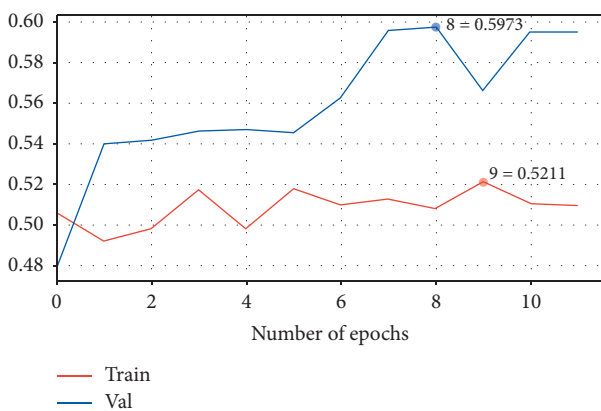


FIGURE 9: The loss learning curve for CNN Model 1.

shown in Figures 10 and 11, respectively. However, as shown in Figure 11, the validation score is consistently less than the training score, with the suspicion that this model suffers from bias [19].

3.4. Predicting Invasive Cancer Using CNN Model 3. CNN Model 3 is deeper than Models 1 and 2, with a five-layer CNN used to detect breast cancer [37]. This architecture gives the best result with 87% accuracy as shown in Table 6: it also provides a similar distribution of predicted labels to that of actual labels (50/50). Table 7 shows the configuration summary of Model 3. The confusion matrix and the loss learning curve are shown in Figures 12 and 13, respectively.

TABLE 4: The metric results of CNN Model 2.

| | Precision | Recall | F1-score | Support |
|----------|-----------|--------|----------|---------|
| IDC (-) | 0.72 | 0.91 | 0.81 | 596 |
| IDC (+) | 0.85 | 0.60 | 0.70 | 514 |
| Accuracy | | | 0.76 | 1110 |

TABLE 5: The summary table of CNN Model 2.

| Layer | Type | Output shape | Param. |
|------------------------------|-------------|------------------|---------|
| conv2d_2 | Conv2D | None, 50, 50, 32 | 896 |
| conv2d_3 | Conv2D | None, 50, 50, 32 | 9248 |
| max_pooling2d_1 | MaxPooling2 | None, 25, 25, 32 | 0 |
| batch_normalization | BatchNo | None, 25, 25, 32 | 128 |
| dropout_2 | Dropout | None, 25, 25, 32 | 0 |
| conv2d_4 | Conv2D | None, 25, 25, 64 | 18496 |
| conv2d_5 | Conv2D | None, 25, 25, 64 | 36928 |
| max_pooling2d_2 | MaxPooling2 | None, 12, 12, 64 | 0 |
| batch_normalization_1 | BatchNo | None, 12, 12, 64 | 256 |
| dropout_3 | Dropout | None, 12, 12, 64 | 0 |
| conv2d_6 | Conv2D | None, 12, 12, 86 | 49622 |
| conv2d_7 | Conv2D | None, 12, 12, 86 | 66650 |
| max_pooling2d_3 | MaxPooling2 | None, 6, 6, 86 | 0 |
| batch_normalization_2 | Batch | None, 6, 6, 86 | 344 |
| dropout_4 | Dropout | None, 6, 6, 86 | 0 |
| flatten_1 | Flatten | None, 3096 | 0 |
| dense_2 | Dense | None, 512 | 1585664 |
| dropout_5 | Dropout | None, 512 | 0 |
| dense_3 | Dense | None, 2 | 1026 |
| Total params.: 1,769,258 | | | |
| Trainable params.: 1,768,894 | | | |
| Nontrainable params.: 364 | | | |

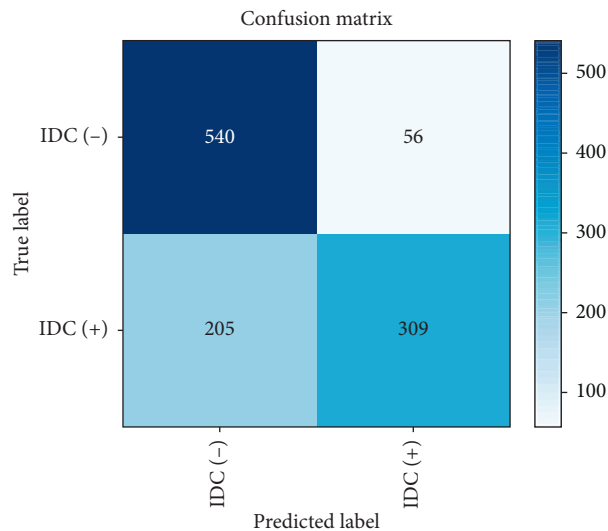


FIGURE 10: The confusion matrix of CNN Model 2.

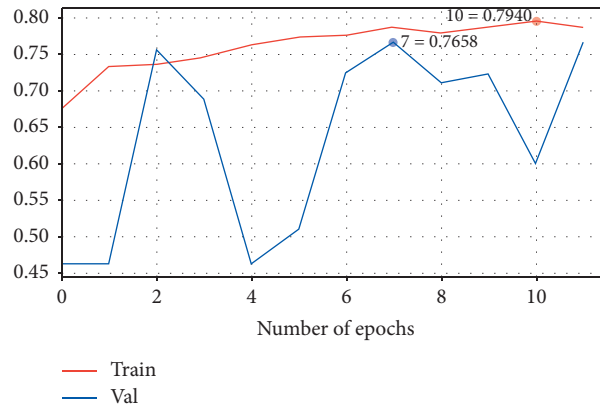


FIGURE 11: The loss learning curve for Model 2.

TABLE 6: CNN Model 3 metric results.

| | Precision | Recall | F1-score | Support |
|----------|-----------|--------|----------|---------|
| IDC (-) | 0.82 | 0.92 | 0.91 | 596 |
| IDC (+) | 0.86 | 0.76 | 0.85 | 514 |
| Accuracy | | | 0.87 | 1110 |

TABLE 7: CNN Model 3 layers.

| Layer | Type | Output shape | Param. |
|---------------------------|------------|------------------|--------|
| conv2d_20 | Conv2D | None, 46, 46, 32 | 2432 |
| max_pooling2d_10 | MaxPooling | None, 15, 15, 32 | 0 |
| conv2d_21 | Conv2D | None, 11, 11, 32 | 25632 |
| max_pooling2d_11 | MaxPooling | None, 3, 3, 32 | 0 |
| dropout_14 | Dropout | None, 3, 3, 32 | 0 |
| flatten_4 | Flatten | None, 288 | 0 |
| dense_8 | Dense | None, 64 | 18496 |
| dropout_15 | Dropout | None, 64 | 0 |
| dense_9 | Dense | None, 2 | 130 |
| Total params.: 46,690 | | | |
| Trainable params.: 46,690 | | | |
| Nontrainable params.: 0 | | | |

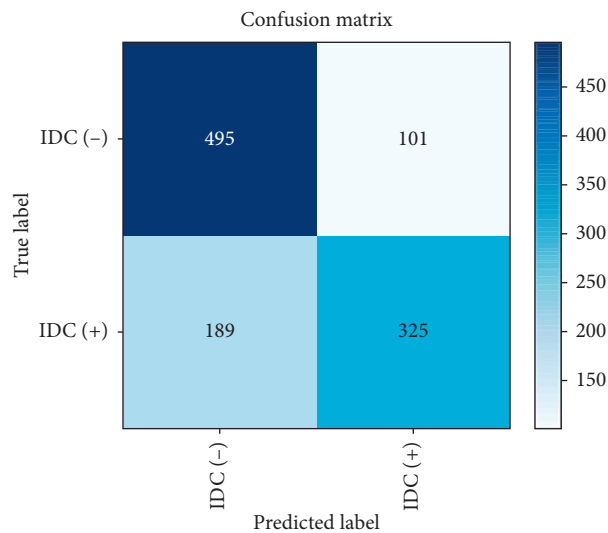


FIGURE 12: Confusion matrix of CNN Model 3.

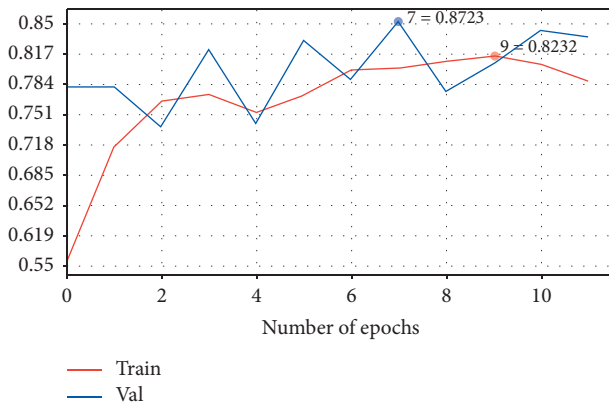


FIGURE 13: Loss learning curve for Model 3.

4. Conclusions

Automating the detection of breast cancer to enhance the care of patients is a challenging task. The current study proposes a CNN approach that analyzes the IDC tissue regions in WSIs for the automatic detection of this cancer. Three different CNN architectures have been described in this paper with a proper comparison. The proposed system using CNN Model 3 achieves 87% accuracy. Although Model 3 is deeper than Models 1 and 2, the five-layer CNN in Model 3 is best suited for this task. All architectures were guided by a big dataset of about 275,000, 50×50 -pixel RGB image patches. When we compared the proposed model with the machine learning (ML) algorithm, the proposed model improved accuracy by 8% over the result of the algorithm. The proposed model was found to successfully obtain correct results that might decrease human mistakes in the diagnosis process and reduce the cost of cancer diagnosis. The main limitation of this study is to use the secondary database like Kaggle, and future study should be done based on primary data for more accuracy of the results related to breast cancer identification.

Data Availability

Datasets analyzed in this study are publicly available. These data can be found at <http://www.andrewjanowczyk.com/use-case-6-invasive-ductal-carcinoma-idc-segmentation/>.

Conflicts of Interest

The authors declare that they have no conflicts of interest.

Acknowledgments

The authors extend their appreciation to the Deanship of Scientific Research at Jouf University for funding this work through Research Grant no. DSR2020-04-489.

References

[1] M. Masud, A. E. Eldin Rashed, and M. S. Hossain, "Convolutional neural network-based models for diagnosis of

breast cancer," *Neural Computing and Applications*, vol. 5, 2020.

- [2] G. Muhammad, M. S. Hossain, and N. Kumar, "EEG-based pathology detection for home health monitoring," *IEEE Journal on Selected Areas in Communications*, vol. 39, no. 2, pp. 603–610, 2021.
- [3] M. Chen, J. Yang, L. Hu, M. S. Hossain, and G. Muhammad, "Urban healthcare big data system based on crowdsourced and cloud-based air quality indicators," *IEEE Communications Magazine*, vol. 56, no. 11, pp. 14–20, 2018.
- [4] M. S. Hossain, "Cloud-supported cyber-physical localization framework for patients monitoring," *IEEE Systems Journal*, vol. 11, no. 1, pp. 118–127, 2017.
- [5] S. A. Alanazi, M. M. Kamruzzaman, M. Alruwaili, N. Alshammari, S. A. Alqahtani, and A. Karime, "Measuring and preventing COVID-19 using the SIR model and machine learning in smart health care," *Journal of Healthcare Engineering*, vol. 2020, Article ID 8857346, 12 pages, 2020.
- [6] Y. Zhang, X. Ma, J. Zhang, M. S. Hossain, G. Muhammad, and S. U. Amin, "Edge intelligence in the cognitive internet of things: improving sensitivity and interactivity," *IEEE Network*, vol. 33, no. 3, pp. 58–64, 2019.
- [7] M. M. Kamruzzaman, "Architecture of smart health care system using artificial intelligence," in *Proceedings of the 2020 IEEE International Conference on Multimedia & Expo Workshops (ICMEW)*, pp. 1–6, London, UK, July 2020.
- [8] W. Min, B.-K. Bao, C. Xu, and M. S. Hossain, "Cross-platform multi-modal topic modeling for personalized inter-platform recommendation," *IEEE Transactions on Multimedia*, vol. 17, no. 10, pp. 1787–1801, 2015.
- [9] M. M. Kamruzzaman, "Arabic sign language recognition and generating Arabic speech using convolutional neural network," *Wireless Communications and Mobile Computing*, vol. 2020, Article ID 3685614, 9 pages, 2020.
- [10] M. S. Hossain, S. U. Amin, M. Alsulaiman, and G. Muhammad, "Applying deep learning for epilepsy seizure detection and brain mapping visualization," *ACM Transactions on Multimedia Computing, Communications, and Applications*, vol. 15, no. 1, pp. 1–17, 2019.
- [11] J. L. Wang, A. K. Ibrahim, H. Zhuang, A. Muhamed Ali, A. Y. Li, and A. Wu, "A study on automatic detection of IDC breast cancer with convolutional neural networks," in *Proceedings of the 2018 International Conference on Computational Science and Computational Intelligence (CSCI)*, pp. 703–708, Las Vegas, NV, USA, December 2018.
- [12] M. S. Hossain and G. Muhammad, "Emotion-aware connected healthcare big data towards 5G," *IEEE Internet of Things Journal*, vol. 5, no. 4, pp. 2399–2406, 2018.
- [13] A. Cruz-Roa, A. Basavanthally, F. González et al., "Automatic detection of invasive ductal carcinoma in whole slide images with convolutional neural networks," *Medical Imaging 2014: Digital Pathology*, vol. 9041, no. 216, p. 904103, 2014.
- [14] S. U. Amin, M. Alsulaiman, G. Muhammad, M. A. Bencherif, and M. S. Hossain, "Multilevel weighted feature fusion using convolutional neural networks for EEG motor imagery classification," *IEEE Access*, vol. 7, pp. 18940–18950, 2019.
- [15] N. Wahab and A. Khan, "Multifaceted fused-CNN based scoring of breast cancer whole-slide histopathology images," *Applied Soft Computing*, vol. 97, p. 106808, 2020.
- [16] M. Gravina, S. Marrone, M. Sansone, and C. Sansone, "DAE-CNN: exploiting and disentangling contrast agent effects for breast lesions classification in DCE-MRI," *Pattern Recognition Letters*, vol. 145, pp. 67–73, 2021.

- [17] L. Tsochatzidis, P. Koutla, L. Costaridou, and I. Pratikakis, "Integrating segmentation information into CNN for breast cancer diagnosis of mammographic masses," *Computer Methods and Programs in Biomedicine*, vol. 200, p. 105913, 2021.
- [18] M. Malathi, P. Sinthia, F. Farzana, and G. Aloy Anuja Mary, "Breast cancer detection using active contour and classification by deep belief network," *Materials Today: Proceedings*, 2021.
- [19] M. Desai and M. Shah, "An anatomization on breast cancer detection and diagnosis employing multi-layer perceptron neural network (MLP) and Convolutional neural network (CNN)," *Clinical eHealth*, vol. 4, pp. 1–11, 2021.
- [20] D. Abdelhafiz, J. Bi, R. Ammar, C. Yang, and S. Nabavi, "Convolutional neural network for automated mass segmentation in mammography," *BMC Bioinformatics*, vol. 21, no. 1, pp. 1–19, 2020.
- [21] H. Rezaeilouyeh, A. Mollahosseini, and M. H. Mahoor, "Microscopic medical image classification framework via deep learning and shearlet transform," *Journal of Medical Imaging*, vol. 3, no. 4, Article ID 044501, 2016.
- [22] G. Murtaza, L. Shuib, A. W. Abdul Wahab et al., "Deep learning-based breast cancer classification through medical imaging modalities: state of the art and research challenges," *Artificial Intelligence Review*, vol. 53, no. 3, pp. 1655–1720, 2020.
- [23] M. F. Alhamid, M. Rawashdeh, H. Al Osman, M. S. Hossain, and A. El Saddik, "Towards context-sensitive collaborative media recommender system," *Multimedia Tools and Applications*, vol. 74, no. 24, pp. 11399–11428, 2015.
- [24] S. Qian, T. Zhang, C. Xu, and M. S. Hossain, "Social event classification via boosted multimodal supervised latent dirichlet allocation," *ACM Transactions on Multimedia Computing, Communications, and Applications*, vol. 11, no. 2, pp. 1–22, 2015.
- [25] D. Singh, S. Singh, M. Sonawane, R. Batham, and P. A. Satpute, "Breast cancer detection using convolution neural network," *International Research Journal of Engineering and Technology*, vol. 5, no. 6, pp. 316–318, 2017.
- [26] P. Kumar, S. Srivastava, R. K. Mishra, and Y. P. Sai, "End-to-end improved convolutional neural network model for breast cancer detection using mammographic data," *The Journal of Defense Modeling and Simulation: Applications, Methodology, Technology*, Article ID 154851292097326, 2020.
- [27] M. Alhussein, G. Muhammad, M. S. Hossain, and S. U. Amin, "Cognitive IoT-cloud integration for smart healthcare: case study for epileptic seizure detection and monitoring," *Mobile Networks and Applications*, vol. 23, no. 6, pp. 1624–1635, 2018.
- [28] A. Janowczyk, "Use case 6: invasive ductal carcinoma (IDC) segmentation," 2015, <http://www.andrewjanowczyk.com/use-case-6-invasive-ductal-carcinoma-idc-segmentation/>.
- [29] M. S. Hossain, G. Muhammad, and N. Guizani, "Explainable AI and mass surveillance system-based healthcare framework to combat COVID-19 like pandemics," *IEEE Network*, vol. 34, no. 4, pp. 126–132, 2020.
- [30] S. Z. Ramadan, "Using convolutional neural network with cheat sheet and data augmentation to detect breast cancer in mammograms," *Computational and Mathematical Methods in Medicine*, vol. 2020, Article ID 9523404, 9 pages, 2020.
- [31] M. Mehmood, E. Ayub, F. Ahmad et al., "Machine learning enabled early detection of breast cancer by structural analysis of mammograms," *Computers, Materials and Continua*, vol. 67, no. 1, pp. 641–657, 2021.
- [32] C. Shorten and T. M. Khoshgoftaar, "A survey on image data augmentation for deep learning," *Journal of Big Data*, vol. 6, no. 1, p. 60, 2019.
- [33] S. U. Amin, M. Alsulaiman, G. Muhammad, M. A. Mekhtiche, and M. Shamim Hossain, "Deep learning for EEG motor imagery classification based on multi-layer CNNs feature fusion," *Future Generation Computer Systems*, vol. 101, pp. 542–554, 2019.
- [34] D. C. Cireşan, A. Giusti, L. M. Gambardella, and J. Schmidhuber, "Mitosis detection in breast cancer histology images with deep neural networks," *Medical Image Computing and Computer-Assisted Intervention*, vol. 8150, no. 2, pp. 411–418, 2013.
- [35] M. S. Hossain, G. Muhammad, and A. Alamri, "Smart healthcare monitoring: a voice pathology detection paradigm for smart cities," *Multimedia Systems*, vol. 25, no. 5, pp. 565–575, 2019.
- [36] M. Nawaz, A. A. Sewissy, and T. H. A. Soliman, "Multi-class breast cancer classification using deep learning convolutional neural network," *International Journal of Advanced Computer Science and Applications*, vol. 9, no. 6, pp. 316–322, 2018.
- [37] Y. Zhang, S. Chan, V. Youngjean Park et al., "Automatic detection and segmentation of breast cancer on MRI using mask R-CNN trained on non-fat-sat images and tested on fat-sat images," *Academic Radiology*, pp. 1–10, 2020.